Nuclear Engineering and Technology 52 (2020) 2346–2352

Contents lists available at ScienceDirect

Nuclear Engineering and Technology

journal homepage: www.elsevier.com/locate/net

Original Article

Feasibility study of SiPM based scintillation detector for dual-energy X-ray absorptiometry

Chanwoo Park [a], Hankyeol Song [a], Jinhun Joung [b], Yongkwon Kim [b], Kyu Bom Kim [c, d, **], Yong Hyun Chung [a, *]

[a] Department of Radiation Convergence Engineering, College of Health Science, Yonsei University, Wonju, Republic of Korea
[b] Nucare. Inc., Incheon, Republic of Korea
[c] Department of Neurosurgery, Yonsei University College of Medicine, Republic of Korea
[d] Department of Integrative Medicine, Major in Digital Healthcare, Yonsei University, Republic of Korea

ARTICLE INFO

Article history:
Received 6 February 2020
Received in revised form
27 March 2020
Accepted 30 March 2020
Available online 3 April 2020

Keywords:
Dual-energy x-ray absorptiometry (DXA)
Silicon photomultipliers (SiPM)
LYSO Scintillation crystal

ABSTRACT

Dual-energy x-ray absorptiometry (DXA) is the noninvasive method to diagnose osteoporosis disease characterized by low bone mass and deterioration of bone tissue. Many global companies and research groups have developed the various DXA detectors using a direct photon-counting detector such as a cadmium zinc telluride (CZT) sensor. However, this approach using CZT sensor has some drawback such as the limitation of scalability by high cost and the loss of efficiency due to the requirement of a thin detector.

In this study, a SiPM based DXA system was developed and its performance evaluated experimentally. The DXA detector was composed of a SiPM sensor coupled with a single LYSO scintillation crystal ($3 \times 3 \times 2$ mm^3). The prototype DXA detector was mounted on the dedicated front-end circuit consisting of a voltage-sensitive preamplifier, pulse shaping amplifier and constant fraction discriminator (CFD) circuit. The SiPM based DXA detector showed the 34% (at 59 keV) energy resolution with good BMD accuracy. The proposed SiPM based DXA detector showed the performance comparable to the conventional DXA detector based on CZT.

1. Introduction

Bone mineral density (BMD) measurements are used to diagnose osteoporosis disease and to assess the deterioration of bone tissue which increases the risk of fracture. It can also be used to monitor the treatment progress and to assess skeletal changes over age [1,3].

Dual-energy x-ray absorptiometry (DXA) is a non-invasive imaging technique useful for measuring BMD. The DXA has various advantages of short scan times, easy setup of patients for scanning, low radiation dose, and good measurement accuracy. Based on some advantages, DXA equipment was selected as a worldwide reference device for BMD measurement by the World Health Organization (WHO) [1–3,22,23].

Early DXA detectors were consist of photomultiplier tube (PMT)-based counting detector systems. The trend in recent DXA instruments is to use CZT (CdZnTe) sensors that can measure accurate BMD with low exposures [5,6]. CZT sensors are stable crystalline compounds formed of cadmium, zinc, and tellurium, of which spectral resolution outperforms commercially available scintillation crystals [7,8]. DXA detectors using CZT sensors do not require a scintillator and are advantageous for energy resolution and spatial resolution, however, they suffer from limitations such as scalability due to high cost and efficiency losses due to thin detector requirements [9,10]. In addition, the detector requires a large number of read-out channels, the performance of which is affected by the applied voltage.

Recently, Silicon photomultipliers (SiPMs) has made great progress and success with the high performance such as high detection efficiency, low dark count rate and high sensor gain [11–15]. LYSO scintillation crystal also achieve high light output,

* Corresponding author. 1 Yonseidae-gil, Department of Radiation Convergence Engineering, College of Health Science, Yonsei University, Heungup, Wonju, Gangwondo, 220–710, Republic of Korea.
** Corresponding author. Yonsei University College of Medicine, 20 Eonju-ro 63-gil, Gangnam-gu, Seoul, 06229, Republic of Korea.
E-mail addresses: ssmakal@yuhs.ac, ssmakal@yuhs.ac.kr (K.B. Kim), ychung@yonsei.ac.kr (Y.H. Chung).

https://doi.org/10.1016/j.net.2020.03.030

short rise time, and short decay time [16]. The SiPM detector coupled with LYSO has similar sensitivity to CZT, and is sufficient as a detector for bone density measurement.

The purpose of this study is to develop a SiPM based DXA detector and to experimentally evaluate its performance. The DXA detector was designed by implementing a SiPM coupled with a single LYSO crystal ($3 \times 3 \times 2$ mm^3). The energy resolution was measured using an isotope radiation source (Am-241 (59 keV)) to compare the performance at the very low radiation energy of the X-ray detector according to different detectors (SiPM and CZT). In order to estimate the detection accuracy of x-ray filtered with a K-edge filter, the energy spectra of two detectors (SiPM and CZT) were measured using x-ray generator. In addition, extracted attenuation maps were obtained to evaluate the detector count linearity depending on the various density for different materials.

2. Materials and methods

2.1. Dual x-ray detector module configuration

2.1.1. Prototype SiPM based DXA detector

As shown in Fig. 1, the DXA detector consists of a single LYSO scintillation crystal (Epic-Crystal, China) of $3 \times 3 \times 2$ mm^3 and a single pixel SiPM (MPPC, S13360-3050 PE, Hamamatsu, Japan). All polished crystal surfaces except surface coupling SiPM were covered with 4 layers of Teflon tape. The SiPM consists of a matrix of thousands microcells (50 μm × 50 μm) operated at a breakdown voltage of about 56.0 V. The SiPM case dimension were 3.4×3.4 mm^2 and active area was 3×3 mm^2. The optical grease (Saint-Gobain Crystals, Hiram, USA) was used between LYSO scintillation crystal and SiPM to improve photon transfer effectiveness.

2.1.2. Analog signal processing and front-end electronics

Fig. 2 shows a readout structure that includes a front-end electronics consisting of a preamplifier, pulse shaping amplifier, peak-sensing trigger circuit, and data acquisition (DAQ). The output signal from the DXA detector is amplified by a preamplifier (AD8039ART, Analog Devices, USA). The preamplifier is a low noise (8 nV/Hz) and 350 MHz bandwidth single amplifier with adjustable gain from 0 to 10 times in a single range. The amplified signals are shaped by the shaping amplifier to alleviate the pile-up problem. To generate the trigger for the peak-sensing on the shaped signal, the peak-sensing trigger circuit employs a constant fraction discriminator (CFD) circuit with a delay of 500 ns after the shaping amplifier. The CFD circuit generates the bipolar signal by multiplying the delayed signal and inverted signal. The zero-crossing point in the bipolar signal is the pickoff time point and the bipolar signal is fed to the comparator. The delay component (DS1100Z-500+, Maxim Integrated, USA) delays the comparator output signal by the rising time of the shaped signal to use the start trigger of the peak sensing analog-to-digital converter (ADC).

2.1.3. Back-end data acquisition (DAQ)

The NI-DAQ was used to acquire the detector readout data. The front-end electronics are connected to a PXI-1033 controller (National Instruments, Austin, TX, USA). The shaped signal and the peak-sensing trigger of the front-end electronics are fed to NI-DAQ (8-channel, 16-bit ADCs, maximum sampling rate of 250 kS/s) [18–20]. The energy information was measured from the height of an analog pulses at the peaks and converted into digital outputs. The digital output is a proportional representation of the analog pulse height in the shaped input signal [21]. The PXI controller handles the command transfer to the computer interface modules along with the desktop running LABVIEW. The PXI controller was installed on one data acquisition card, NI PXI-6143, (National Instruments, Austin, TX, USA) to simultaneously record input signals. Fig. 3 shows the components of the DXA detector module, including front-end electronics and DAQ.

2.2. Experimental setup

2.2.1. DXA generator setup

Fig. 4 represents the experimental setup of an x-ray tube and DXA detectors for performance evaluation. An x-ray tube with a pencil beam collimator was used. The intensity of the x-ray photon flux was determined by the current at the x-ray tube anode. In this experiment, the tube anode current and the tube voltage were set to 1 mA and 83 kVp, respectively. The distance between the detector and the x-ray tube was 75 cm, and the x-ray passed through a 1 mm thick samarium filter with K-edge absorption at 46.8 keV. The experiment was performed at room temperature of 20°. Dual x-ray photons generated using the samarium K-edge filter were distinguished into low and high energy regions. The theoretical average energies in the low and high energy regions are 38 keV and 65 keV, respectively.

2.2.2. Measurement of energy spectrum

The SiPM detector was used to measure the spectrum of x-rays that passed through the samarium filter. For comparison, a CZT detector used in a commercial DXA equipment (DEXXUM-T, Osteosys) was used under the same conditions. To evaluate the energy resolution of the detectors, the gamma-ray spectra of the two detectors were measured using an Am-241 source that emits 59 keV gamma rays. The energy resolution was estimated by the Gaussian fitting and the full width at half maximum (FWHM) of the 59 keV photo-peak.

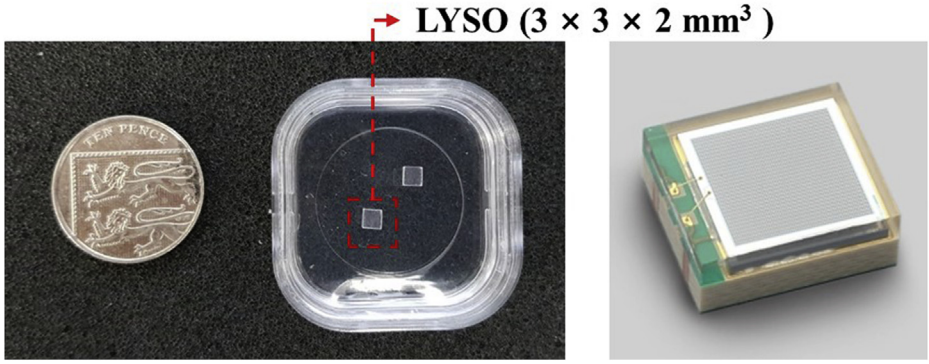

Fig. 1. A $3 \times 3 \times 2$ mm^3 of LYSO scintillation crystal (Epic-Crystal, China) and single pixel of SiPM (MPPC, S13360-3050 PE, Hamamatsu, Japan).

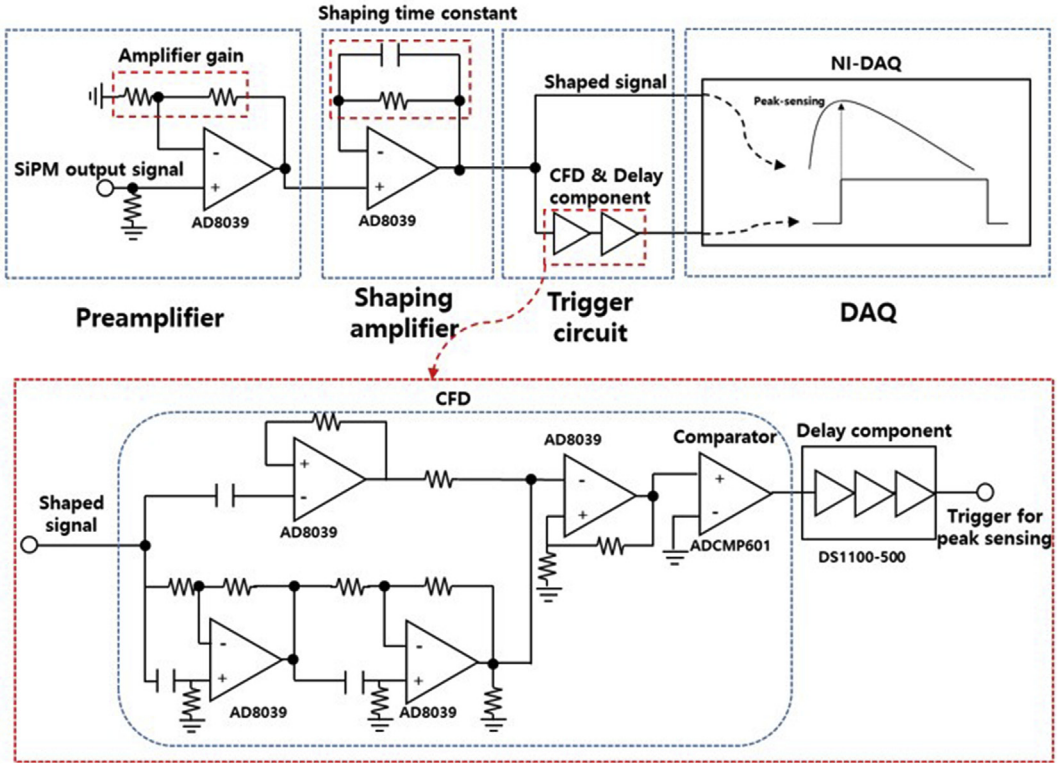

Fig. 2. Schematic diagram of front-end electronics and the peak-sensing ADC. The front-end electronics includes preamplifiers, shaping amplifiers, and trigger circuits. The output of the front-end electronics is fed to the peak-sensing ADC in NI-DAQ to measure energy values.

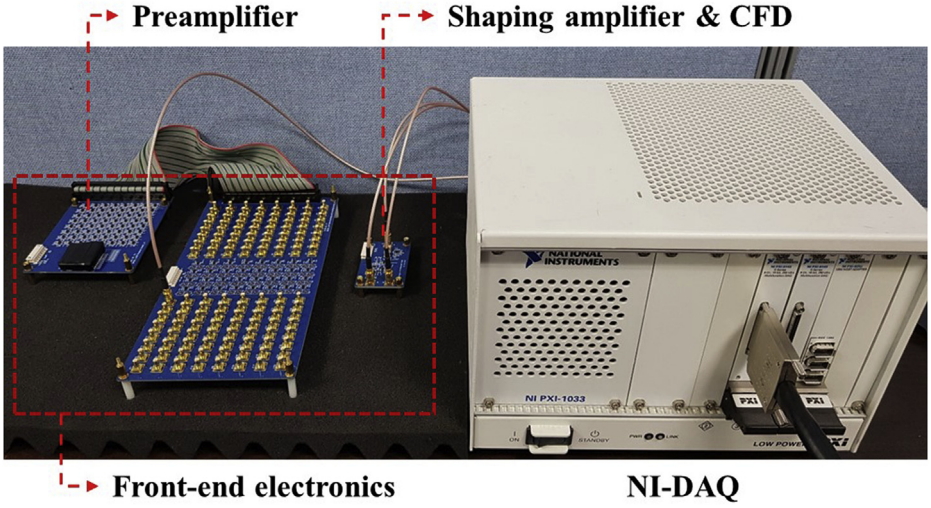

Fig. 3. Components of the DXA detector module including front-end electronics and NI-DAQ.

2.2.3. Evaluation of the accuracy of bone mass measurement

The factor that quantitatively assesses bone mass is bone mineral density (BMD), estimated by calculating the area density (g/cm^2). To evaluate the accuracy of the area density (g/cm^2), aluminum plates (Al plate) and water phantom were used. The attenuation coefficients of Al plate, water, bone tissue and soft tissue at 50 keV are 0.3681 cm^2/g, 0.2269 cm^2/g, 0.3506 cm^2/g, and 0.2264 cm^2/g, respectively [22].

The thickness corresponding to the theoretical area density of the Al plates used in the experiments were 2 mm (0.54 g/cm^2), 4 mm (1.08 g/cm^2) and 6 mm (1.62 g/cm^2), indicating osteoporosis, normal, and BMD excess, respectively. The area density measurement was performed by placing Al plates in a 150 mm deep water phantom considering the thickness of the human upper body, as shown in Fig. 5 [17]. The area density was measured at 9 different locations at 3 mm intervals: the first three with air, the second three with water representing soft tissue, and the last three with water + Al plate representing the soft and bone tissue.

The area density (g/cm^2) of the Al plate was calculated by analyzing the number of detected photons and the attenuation

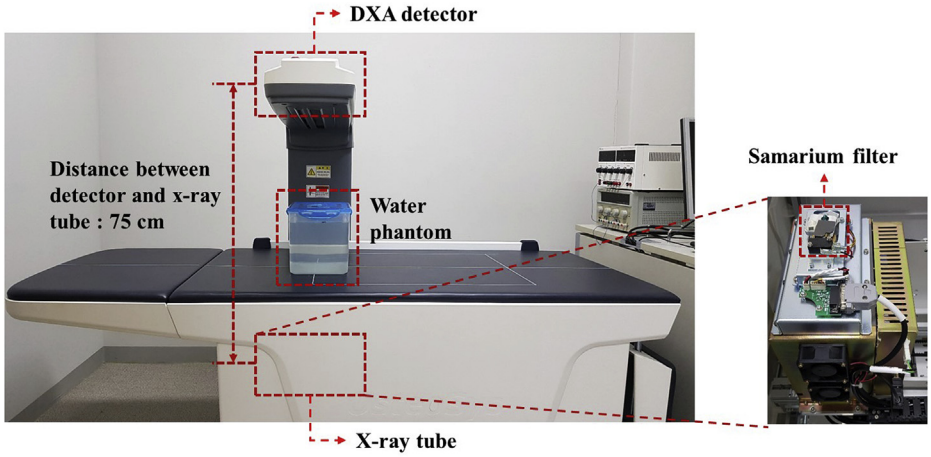

Fig. 4. Experimental Setup of an X-ray tube and DXA detectors for performance evaluation.

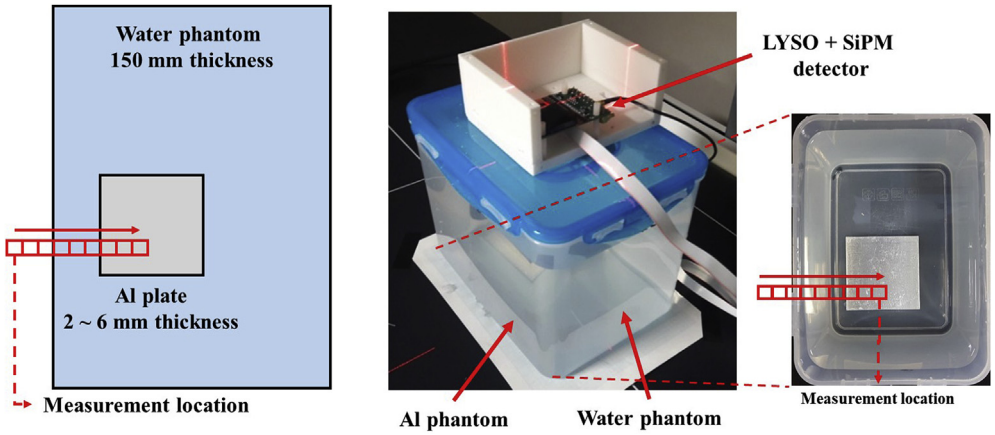

Fig. 5. Experiment setup of measuring the area density for evaluating BMD measurement accuracy.

coefficient of aluminum used as a bone equivalent material [23,24].

$$\textbf{Area density}\left(\mathbf{g}/\mathbf{cm}^2\right) = \ln\left(\frac{\mathbf{I^L}}{\mathbf{I_0^L}}\right) - \mathbf{K}\times\ln\left(\frac{\mathbf{I^H}}{\mathbf{I_0^H}}\right) \Big/ \left(\mu_{\mathbf{Al}}^{\mathbf{L}} - \mathbf{K}\mu_{\mathbf{Al}}^{\mathbf{H}}\right)$$

$$\textbf{Weighting factor}(\mathbf{K}) = \ln\left(\frac{\mathbf{I^L}}{\mathbf{I_0^L}}\right) \Big/ \ln\left(\frac{\mathbf{I^H}}{\mathbf{I_0^H}}\right) \textbf{in water} \quad (1)$$

I_0^L and I^L are the number of detected photons in the low-energy window, with or without the target material, respectively. I_0^H and I^H are the number of detected photons in the high energy window, with or without the target material, respectively. μ_{Al}^L and μ_{Al}^H are the attenuation coefficient of aluminum at the average energy of the low and high energy window, respectively.

2.2.4. Evaluation of contrast-to-noise-ratio

To assess the material decomposition capability, an attenuation map of the phantom was generated and contrast-to-Noise Ratio (CNR) was analyzed in two different energy windows. The attenuation maps in each energy window (Low:$\ln\left(\frac{I^L}{I_0^L}\right)$ and High$\ln\left(\frac{I^H}{I_0^H}\right)$) were obtained using the detected x-ray photons, classified into low and high energy according to the measured energy. To acquire the attenuation map of Al plate only, the decomposed attenuation map (DEC) was obtained using the difference between the low energy attenuation map and the corrected high energy attenuation map using equation (2). The high energy attenuation map ($K\times\ln\left(\frac{I^H}{I_0^H}\right)$) was corrected by weighting factor (K), the ratio of the Low and the High attenuation map measured with water only [23–25].

$$\textbf{Decomposed attenuation map (DEC)} = \ln\left(\frac{\mathbf{I^L}}{\mathbf{I_0^L}}\right) - \mathbf{K}\times\ln\left(\frac{\mathbf{I^H}}{\mathbf{I_0^H}}\right)$$

$$\textbf{Weighting factor}\ (\mathbf{K}) = \ln\left(\frac{\mathbf{I^L}}{\mathbf{I_0^L}}\right) \Big/ \ln\left(\frac{\mathbf{I^H}}{\mathbf{I_0^H}}\right) \textbf{in water} \quad (2)$$

Region-of-interests (ROIs) were set for each Al plate thickness and the CNR was calculated as follows:

$$\mathbf{CNR} = \left(\boldsymbol{ROI_{mean(a)}} - \boldsymbol{ROI_{mean(b)}}\right) \Big/ \boldsymbol{\sigma_{background}} \quad (3)$$

$ROI_{mean(a)}$ and $ROI_{mean(b)}$ are the average values of each ROI, and $\sigma_{background}$ is a standard deviation measured in the background [26,27].

3. Results

3.1. Measurement of energy spectrum

The energy spectra of the CZT and SiPM detector were shown in Fig. 6. The two energy peaks were well distinguished in both detectors. However, the energy spectrum of the CZT detector was slightly narrower than that of the SiPM detector at energy peaks. The 50 keV valley, the boundary between high and low energy due to the samarium filter, was deeper in CZT than SiPM detector. The energy resolution of the CZT and SiPM detector using Am-241 source were shown in Fig. 7. The energy resolutions of the SiPM and CZT detector were 34% and 18% at 59 keV, respectively.

3.2. Evaluation of the accuracy of bone mass measurement

The area density (g/cm^2) was calculated as a function of Al plate thickness ranging from 2 mm to 6 mm, as shown in Fig. 8. The area density values increased linearly with the Al plate thickness. The area density at CZT detector was calculated as 0.5563 g/cm^2, 1.1149 g/cm^2, and 1.6712 g/cm^2, with an Al plate thickness 2, 4, and 6 mm, respectively. Compared with the theoretical area density, the differences were 3.0%, 3.2% and 3.1% for each thickness. In case of SiPM detector, the area density in DEC attenuation map was calculated as 0.5215 g/cm^2, 1.0605 g/cm^2, and 1.5367 g/cm^2 with a Al plate thickness 2, 4, and 6 mm, respectively. Compared with the theoretical area density, the differences were 3.7%, 1.8% and 4.9% for each thickness. The calculated area densities were slightly overestimated in the CZT detector and underestimated in the SiPM detector than the theoretical values.

3.3. Contrast-to-noise ratio measurement

Fig. 9 shows three attenuation maps (High, Low and DEC) measured at various experimental conditions with Al plate thicknesses (2 mm, 4 mm, and 6 mm) to assess the accuracy of BMD.

Fig. 10 represents the calculated CNR for the attenuation maps using the Al plates (2 mm, 4 mm, and 6 mm). Fig. 10(A) and (B) shows the calculated CNR values of the attenuation maps using CZT and SiPM detectors, respectively. The CNR values with the DEC attenuation map showed the better results than those with low or high energy maps, and it means that the Al plate is well decomposed. The CNR values increased linearly with the Al plate thickness.

4. Discussion

The feasibility of a DXA detector based on SiPM coupled with LYSO scintillation crystal was demonstrated by the experiments in this study. The energy spectrum, accuracy of BMD calculation and CNR were measured to compare the performance of DXA detectors with different sensors (SiPM and CZT).

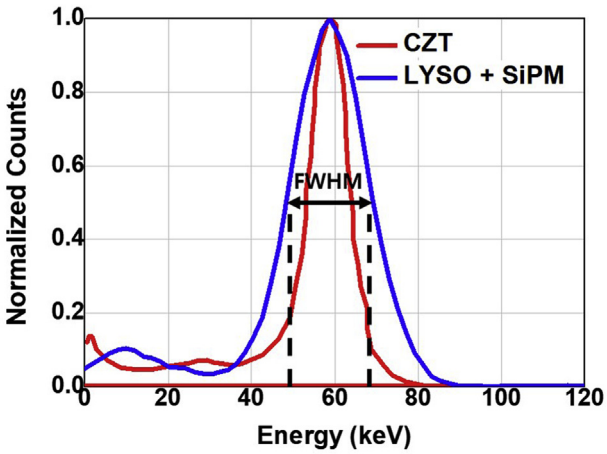

Fig. 7. Energy resolution of CZT and SiPM detector.

The SiPM based DXA detector showed the 34% (at 59 keV) energy resolution with good BMD accuracy (≈3% error rate). The energy resolution of CZT detector is superior to SiPM detector. Conversion efficiency of CZT detectors is superior to SiPM-based detectors because CZT detectors converts radiation directly into electrons [7]. This results in a difference in energy resolution between the CZT and SiPM-based detector. CZT detectors have narrower energy peaks and deeper valleys than SiPM-based detectors. However, the valley of energy resolution of SiPM between two energy peaks was clearly identified. It allows us to separate two different energy regions for BMD calculation, demonstrating the feasibility of SiPM detector for DXA detector. The development of dedicated readout electronics using commercially available low-noise amplifiers that provide wide-band amplification with extremely low noise has enabled to achieve useable energy resolution.

The accuracy in BMD measurement was affected by inhomogeneous distribution of both bone marrow and soft tissue in human body. Therefore, it was necessary to evaluate the BMD accuracy of DXA detector. The area density representing BMD was measured and compared with the theoretically calculated values. The measured and theoretical values matched well within 5% error. The BMD accuracy of this study (~5%) are lower than commercial DXA detector (~1%). However, BMD can be measured with BMD accuracy within 10% according to WHO regulations [28]. The accuracy error in BMD increases with the Al thickness due to the increased

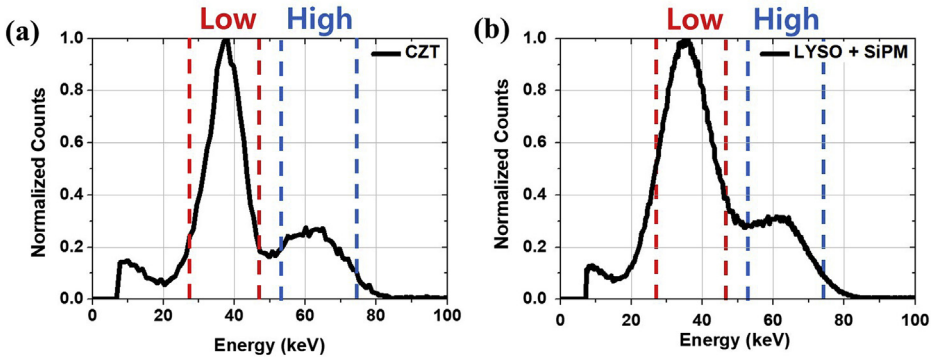

Fig. 6. X-ray spectra (a): CZT detector, (b): SiPM detector.

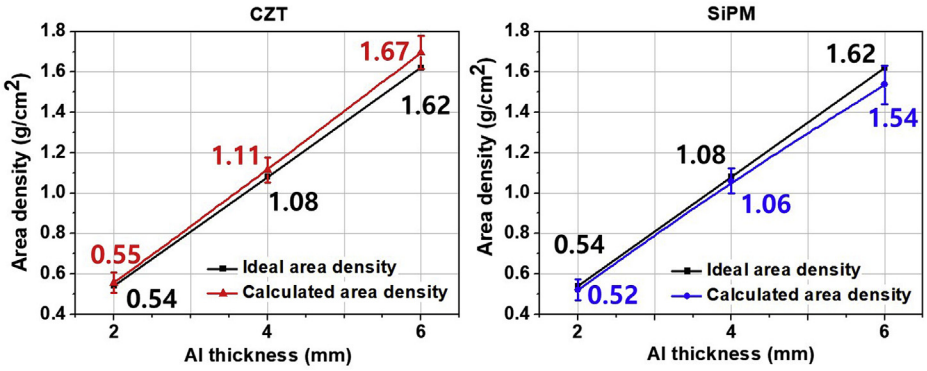

Fig. 8. The theoretically calculated and measured area density as a function of Al thickness.

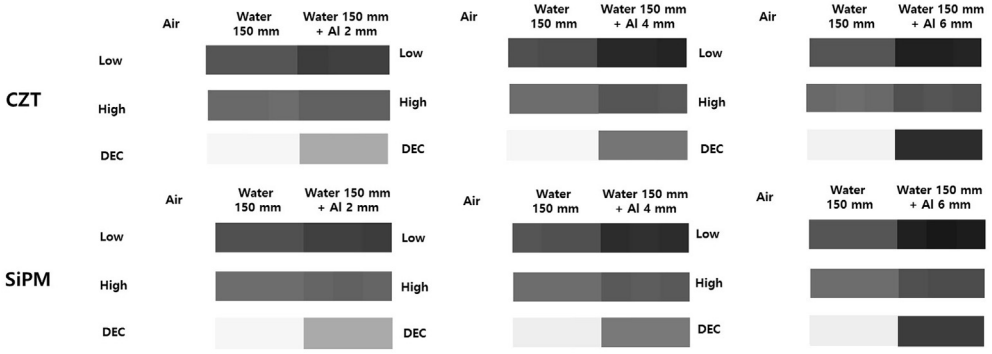

Fig. 9. Attenuation maps of air, water, water + Al plate conditions using CZT and SiPM detector.

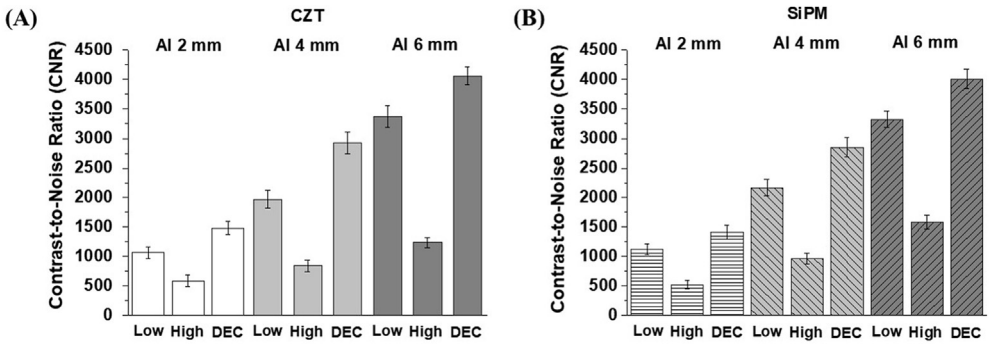

Fig. 10. Calculated CNR values from each attenuation map for Al plate with different thickness.

attenuation and scattering in the path of the X-ray beam. The experiments were performed without considering the beam hardening effect [29]. In further study, studies on improving BMD accuracy by the beam hardening correction will be conducted.

The CNR is a measure used to determine image quality. The CNR of SiPM detector agreed well with the CZT detector under various experimental conditions and it proves that SiPM detector can provide the observer with acceptable image quality. The CNR value increases with the Al thickness because the Al plate acts as the filter to attenuate X-rays.

In this study, the proposed SiPM-based DXA detector showed BMD and CNR performance comparable to CZT based commercial DXA detector. The low cost of SiPM makes it easy to adapt SiPM detectors to wide fan beam scanning DXA system reducing patient dose and scan time to 1 min or less [30,31]. In further study, additional studies will be conducted on the effect of BMD measurements on long time (over 10 min) measurements.

5. Conclusion

This study is a feasibility research of SiPM based scintillation detector for BMD measurements. The SiPM based scintillation detector provides good performance for measuring area density. These results showed that the proposed detector can be used for measuring the BMD.

Acknowledgements

This work was supported by the Nuclear Safety Research Program through the Korea Foundation Of Nuclear Safety (KoFONS)

using the financial resource granted by the Nuclear Safety and Security Commission (NSSC) of the Republic of Korea. (No. 1903013) and the Korea Institute of Energy Technology Evaluation and Planning (KETEP) grant funded by the Korea government (MOTIE) (20161520302180) and Basic Science Research Program through the National Research Foundation of Korea (NRF) funded by the Ministry of Education (NRF-2018R1A6A3A11050877).

References

[1] Glen M. Blake, Ignac Fogelman, The role of DXA bone density scans in the diagnosis and treatment of osteoporosis, Postgrad. Med. 83 (2007) 509–517.
[2] Yong Jun Choi, Byung Joo Lee, Hyun Chae Lim, Yoon-Sok Chung, Cross-calibration of iDXA and prodigy on spine and femur scans in Korean adults, J. Clin. Densitom. 12 (4) (2009) 450–455.
[3] Centers for Disease Control and Prevention National Center for Health Statistics, Dual Energy X-Ray Absorptiometry (DXA) Procedures Manual, 2007. Available from: http://www.cdc.gov/nchs/data/nhanes/nhanes_07_08/manual_dexa.pdf.
[5] Wear James, Michael Buchholz, Randall K. Payne, Darrell Gorsuch, Bisek Joseph, David L. Ergun, Joe Grosholz, Ron Falk, CZT detector for dual-energy x-ray absorptiometry (DEXA), Proc. SPIE 4142, in: International Symposium on Optical Science and Technology, DEC 18, 2000. San Diego, CA, United States.
[6] R.B. Mazess1, J.A. Hanson1, R. Payne1, R. Nord, M. Wilson, Axial and total-body bone densitometry using a narrow-angle fan-beam, Osteoporos. Int. 11 (2000) 158–166.
[7] K. Iniewski, CZT detector technology for medical imaging, J. Inst. Met. 9 (C11001) (2014).
[8] Andrea Zappettini, Laura Marchini, Mingzheng Zha, Giacomo Benassi, Nicola Zambelli, Davide Calestani, Lucio Zanotti, Enos Gombia, Roberto Mosca, Massimiliano Zanichelli, Maura Pavesi, Natalia Auricchio, Ezio Caroli, Growth and characterization of CZT crystals by the vertical bridgman method for X-ray detector applications, IEEE Trans. Nucl. Sci. 58 (5) (2011) 2352–2356.
[9] R.B. James, T.E. Schelinger, J. Lund, M. Schieber, T.E. Schelinger, R.B. James, Semiconductors for Room Temperature Nuclear Detector Applications, Academic Press, New York, 1996.
[10] Jennifer Prekeges, Nuclear Medicine Instrumentation, Jones & Bartlett Publishers, 2010.
[11] P. Buzhan, B. Dolgoshein, L. Filatov, A. Ilyin, V. Kantzerov, V. Kaplin, A. Karakash, F. Kayumov, S. Klemin, E. Popova, S. Smirnov, Silicon photomultiplier and its possible applications, Nucl. Instrum. Methods Phys. Res. A. 504 (2003) 48–52.
[12] M. Moszynski, M. Szawlowski, M. Kapusta, M. Balcerzyk, Avalanche photodiodes in scintillation detection, Nucl. Instrum. Methods Phys. Res. A. 497 (2003) 226–233.
[13] E.A. Babichev, S.E. Baru, D.N. Grigoriev, V.P. Oleynikov, V.V. Porosev, G.A. Savinov, Stephane Callier, SiPM based photon counting detector for scanning digital radiography, J. Inst. Met. 10 (C03002) (2015).
[14] P.K. Lightfoot, G.J. Barker, K. Mavrokoridis, Y.A. Ramachers, N.J.C. Spooner, Characterisation of a silicon photomultiplier device for applications in liquid argon based neutrino physics and dark matter searches, J. Inst. Met. 3 (P10001) (2008).
[15] Hamamatsu photonics, MPPC [Internet], https://www.hamamatsu.com/resources/pdf/ssd/mppc_kapd9005e.pdf, 2017.
[16] G.F. Knoll, Radiation Detection and Measurement, John Wiley & Sons, 1999.
[17] D. Pearson, S.A. Cawte, D.J. Green, A comparison of phantoms for cross-calibration of lumbar spine DXA, Osteoporos. Int. 13 (2002) 948–954.
[18] National Instruments, NI PXI-1033 User Manual [Internet], 2012. Available from, http://www.ni.com/pdf/manuals/371991c.pdf.
[19] National Instruments, NI 6143 Specifications [Internet], 2004. Available from, http://www.ni.com/pdf/manuals/370835a.pdf.
[20] Nathan L. Toner, Ph D Thesis, Data Driven Low-Bandwidth Intelligent Control of a Jet Engine Combustor, Purdue University, 2015.
[21] Alan Owens, Semiconductor Radiation Detectors, CRC Press, 2019.
[22] John H. Hubbell, Stephen M. Seltzer, Tables of X-Ray Mass Attenuation Coefficients and Mass Energy-Absorption Coefficients 1 keV to 20 MeV for Elements Z= 1 to 92 and 48 Additional Substances of Dosimetric Interest. No. PB-95-220539/XAB; NISTIR-5632, National Inst. of Standards and Technology-PL, Gaithersburg, MD, 1995 (United States). Ionizing Radiation Div.
[23] K. Harry, Genant, Giuseppe Guglielmi, Michael Jergas, Bone Densitometry and Osteoporosis, Springer Berlin Heidelberg, 2011.
[24] Glen M. Blake, Heinz W. Wahner, Ignac Fogelman, Evaluation of Osteoporosis, Taylor & Francis, 1998.
[25] G.M. Blake, I. Fogelman, Technical principles of dual energy X-ray absorptiometry, Semin. Nucl. Med. 27 (3) (1997) 210–228.
[26] Dong-Hoon Lee, Chanwoo Park, Cheol-Ha Baek, Chaeyeong Lee, Seung-Jae Lee, Hankyeol Song, Yong Hyun Chung, Simulation of a gamma-ray computed tomography.
[27] D. Philippov, E. Popova, S. Vinogradov, A. Stifutkin, A. Pleshko, S. Klemin, A. Ilyin, V. Belyaev, D. Besson, M. Vandychev, Development of SiPM-based X-ray counting scanner for human inspection, IEEE Trans. Nucl. Sci. 65 (8) (2018) 2013–2020.
[28] S. Baim, C.R. Wilson, E.M. Lewiecki, M.M. Luckey, R.W. Downs Jr., B.C. Lentle, Precision assessment and radiation safety for dual-energy X-ray absorptiometry: position paper of the International Society for Clinical Densitometry, J. Clin. Densitom. 8 (4) (2005) 371–378.
[29] G.M. Blake, D.B. McKeeney, S.C. Chhaya, P.J. Ryan, I. Fogelman, Dual energy X-ray absorptiometry: the epects of beam hardening on bone density measurements, Med. Phys. 19 (2) (1992) 459–465.
[30] J.M. Soriano, E. Ioannidou, J. Wang, J.C. Thornton, M.N. Horlick, D. Gallagher, S.B. Heymsfield, R.N. Pierson, Pencil-beam vs fan-beam dual-energy X-ray absorptiometry comparisons across four systems, J. Clin. Densitom. 7 (3) (2004) 281–289.
[31] G.M. Blake, J.C. Parker, F.M.A. Buxton, I. Fogelman, Dual x-ray absorptiometry: a comparison between fan beam and pencil beam scans, Br. J. Radiol. 66 (790) (1993) 902–906.